Tuning morphology, composition and oxygen reduction reaction (ORR) catalytic performance of manganese oxide particles fabricated by

Journal of Colloid and Interface Science 583 (2021) 71–79

Contents lists available at ScienceDirect

Journal of Colloid and Interface Science

journal homepage: www.elsevier.com/locate/jcis

Regular Article

Tuning morphology, composition and oxygen reduction reaction (ORR) catalytic performance of manganese oxide particles fabricated by γ-radiation induced synthesis

Zhuofeng Li [a], Yi Yang [a], Axel Relefors [a], Xiangyang Kong [b], Gerard Montserrat Siso [c], Björn Wickman [c], Yohannes Kiros [a], Inna L. Soroka [a,*]

[a] School of Engineering Sciences in Chemistry, Biotechnology and Health, KTH Royal Institute of Technology, S-100 44 Stockholm, Sweden
[b] Institute of Materials for Mobile Energy, School of Mater. Sci. & Eng. Shanghai, Jiao Tong University, Dongchuan Road 800, Shanghai 200240, PR China
[c] Department of Physics, Chalmers University of Technology, SE- 412 96 Gothenburg, Sweden

HIGHLIGHTS

- Manganese oxide nano-catalysts are fabricated by γ-radiation induced method.
- Morphology and composition of MnOx are tuned by the synthesis conditions.
- Oxygen reduction reaction (ORR) activity of the obtained material is studied.
- Hollow spherical γ-MnO_2 particles exhibit a 4-electron transfer pathway.
- Mn_3O_4 (with composition 2MnO-MnO_2) nanorods favour an incomplete 2-electron pathway.

GRAPHICAL ABSTRACT

ARTICLE INFO

Article history:
Received 15 June 2020
Revised 2 September 2020
Accepted 3 September 2020
Available online 8 September 2020

Keywords:
MnOx nanoparticles
γ-radiation induced synthesis
ORR
4-electron transfer

ABSTRACT

A γ-radiation induced synthesis method is used to fabricate manganese oxide catalysts through both reduction and oxidation routes. It is shown that the morphology, composition and electrochemical performance of the produced manganese oxide particles can be tuned by altering the redox conditions. The catalysts prepared *via* radiolytic oxidation have a hollow spherical morphology, possess γ-MnO_2 structure and show high catalytic activity for the complete four-electron reaction pathway of the oxygen reduction reaction (ORR) in alkaline electrolyte. Meanwhile, the catalysts synthesized *via* radiolytic reduction possess a rod-like morphology with a Mn_3O_4 bulk structure and favour the incomplete two-electron reaction pathway for ORR. The high catalytic activity of the manganese oxide synthesized *via* the oxidation route can be attributed to high electrochemical surface area and increased amount of Mn^{3+} on the surface as compared to those in the sample obtained *via* the reduction route.

* Corresponding author.
E-mail address: soroka@kth.se (I.L. Soroka).

https://doi.org/10.1016/j.jcis.2020.09.011
0021-9797/

1. Introduction

Manganese oxides are known for their multiple applications for energy storage and conversion [1–4]. In particular, nanostructured MnO_2 has shown considerable catalytic activity for ORR [5–7]. The electrochemical behaviour of manganese oxide is mainly determined by their structural and surface properties [8]. The basic structural unit of MnO_2 is [MnO_6] octahedrons linked in different ways by sharing edges or corners, thus forming variations in structures [9,10], such as one-dimensional tunnel structure like α-, β- and γ-MnO_2, two-dimensional layered structure like δ-MnO_2 and three-dimensional spinel structure like λ-MnO_2 [3,11–13]. In earlier studies it was shown that catalytic activity of manganese oxide was dependent on their polymorphs and morphology, where ORR catalytic performance was displayed in the following sequence: α-MnO_2 > δ-MnO_2 > γ-MnO_2 > β-MnO_2 [6,14,15]. Meanwhile, α-MnO_2 and β-MnO_2 nanowires showed higher catalytic activities as compared to α-MnO_2 and β-MnO_2 nano-rods [16].

The good electrochemical activity of manganese oxides can be attributed to the redox couple of Mn^{3+}/Mn^{4+} that exists in the octahedral sites with the presence of vacancies in solid phase [8]. The oxygen reduction on a manganese oxide cathode proceeds through chemical oxidation of surface Mn^{3+} ions generated by the discharge of MnO_2 [14] and the total reaction pathway follows a four-electron reduction pathway [17]. In Mn-based compounds, Mn^{3+} ions cause one of the largest Jahn-Teller lattice distortions, whereas Mn^{4+} ion does not contribute much to those distortions [18]. Furthermore, the ability to transfer electrons from Mn^{3+} to the adsorbed oxygen ($O_{2(ad)}$) to form Mn^{4+}–$O_{2(ad)}$ is an important characteristic of the Mn-based catalysts for ORR [19]. Therefore, the electro-catalytic activity for ORR of different types of Mn oxides can be dependent on the amount of accessible Mn^{3+} species on the surface [15].

The ORR performance can be improved by incorporating nanocatalysts on a carbon support that possess high surface area and good conductivity [20,21]. In addition, the synergetic effect can lead to a substantial electron transfer between the supported manganese oxides and carbon, thereby effectively increase the catalytic performance of manganese oxides [22]. The size control and mono-dispersity of nanoparticles has become the main issue and direction in carbon supported nanocomposite fabrication [23,24]. It was shown previously that the structural properties of manganese oxides can be tuned by choosing appropriate synthesis routes [10]. The nanostructured manganese oxides for catalysis applications can be synthesized by for example, sol-gel method [25], co-precipitation method [26], hydrothermal methods [5,15,27,28], wet chemistry methods [11,29], and radiation induced synthesis method [30–32].

During the last decades, γ-radiation induced synthesis of nanomaterials attracted significant attention due to the following advantages: low energy consumption; minimal use of potentially harmful chemicals; relatively simple synthesis schemes [33]. γ-radiation induced synthesis involves redox reactions between products of water radiolysis, radicals and active species, and dissolved metal salt precursors, resulting in precipitation of less soluble reaction products. Since the formation of the radicals stops immediately when the solution is removed from the radioactive source, the amount of reacting radicals and, thus, the amount of obtained precipitate can be controlled by the total radiation dose with high accuracy. As reported in the literature, by varying γ-radiation induced synthesis parameters, such as radiation dose rate, total dose, scavenger concentration, and type of solvents, nanoparticles with different composition, size and morphology can be engineered. Thus, free-standing MnO_2 nano-wires can be produced by γ-radiation induced synthesis method *via* both reductive route, $Mn^{7+} \rightarrow Mn^{4+}$, from $KMnO_4$ precursor solution, and oxidative route, $Mn^{2+} \rightarrow Mn^{4+}$, from Mn (II) salts solutions [31,34–36].

In the current study we apply γ-radiation induced approach to synthesize not only free-standing MnO_x nanomaterials but manganese oxide based nanocatalysts deposited on a carbon support, aiming to substantiate how morphology, composition and catalytic activity of the obtained material can be tuned by the redox conditions. The nanocatalysts are synthesized by using different radiolytic routes: oxidation and reduction. Structural properties of the obtained material and its electrochemical activities for the ORR in alkaline electrolyte were investigated.

2. Experimental

2.1. Radiation induced synthesis of manganese oxide

Radiation induced preparation of metal oxide particles in aqueous solution involves reactions between water radiolysis products and the metal precursor ions. When absorbing ionizing radiation water molecules decompose to form free radicals and molecular species [37]:

$$H_2O \overset{\gamma-\text{radiation}}{\rightarrow} OH^{\cdot}, e^{-}_{aq}, H_3O+, H^{\cdot}, H_2, H_2O_2 \quad (1)$$

Both oxidizing and reducing species are formed in equivalent amounts. The hydrated electron, e^{-}_{aq}, with E^0 (H_2O/e^{-}_{aq}) = -2.87 V_{SHE} can reduce most metal ions to lower valence states [38]. Meanwhile, the hydroxyl radical, $OH^{\bullet}$, is a powerful oxidant, with E^0 ($OH^{\bullet}/H_2O$) = +1.8 V_{SHE} capable to oxidize most metal ions into higher valence state [39]. For radiation induced synthesis, the solution redox condition can be shifted to either reducing or oxidizing conditions by adding the proper radical scavenger before radiation.

Under reducing conditions, $OH^{\bullet}$ radicals are scavenged by isopropanol to produce reducing 2-hydroxyl-2-propyl radical $(CH_3)_2COH^{\bullet}$, E^0 = -1.8 V_{SHE} [40], according to the reaction:

$$HO^{\bullet} + (CH_3)_2CHOH \rightarrow H_2O + (CH_3)_2COH^{\bullet} \quad (2)$$

The interaction of precursor $KMnO_4$ with reducing radicals, e^{-}_{aq} and $(CH_3)_2COH^{\bullet}$ can be described by the following reactions:

$$Mn^{7+} + ne^{-}{}_{aq} \rightarrow Mn^{(7-n)+} \quad (3)$$

$$Mn^{7+} + n(CH_3)_2COH^{\bullet} \rightarrow Mn^{(7-n)+} + (CH_3)_2CO + nH^{+} \quad (4)$$

In oxidizing conditions, N_2O is used to convert e^{-}_{aq} to $OH^{\bullet}$ according to the following reaction:

$$N_2O + e^{-}{}_{aq} + H_2O \rightarrow OH^{\bullet} + OH^{-} + N_2 \quad (5)$$

The formation of MnO_2 colloids by the reaction of $OH^{\bullet}$ with Mn^{2+} ions in solution was described previously [36]. When dissolved in water, Mn^{2+} ions form a hydrated species $[Mn(H_2O)_6]^{2+}$. The formation of MnO_2 can be described by the following overall processes:

$$[Mn(H_2O)_6]^{2+} + 2OH^{\bullet} \rightarrow MnO_2 + 2H^{+} + 6H_2O \quad (6)$$

Note that in both synthesis paths, pH of the solutions after irradiation is usually decreased from almost neutral to acidic (pH 2 to 3) which is attributed to the formation of H^{+} *via* reactions (4) and (6).

Considering the above, manganese ions in oxidation states Mn^{4+} (MnO_2), Mn^{3+} and Mn^{2+} can be formed. Note that one needs 3 reducing species to get one molecule MnO_2 and 4.3 reducing species to get an oxide with mixed valences, such as Mn_3O_4.

Although the solubility of many Mn^{2+} compounds/salts is high, Mn_3O_4 is stable in aqueous solutions [41]. The structure of Mn_3O_4 may have several modifications, such as MnO-Mn_2O_3 (with Mn^{2+} and Mn^{3+}) and 2MnO-MnO_2 (with Mn^{2+} and Mn^{4+}) [42].

2.2. Synthesis condition

Manganese oxide particles both free-standing and on carbon support were obtained by γ-radiation induced synthesis using oxidation and reduction routes. In the oxidation route, Mn^{2+} salt, manganese chloride tetrahydrate, $MnCl_2{\cdot}4H_2O$, (Sigma Aldrich, ≥ 99.9% purity) was used as a precursor, while in the reduction route, Mn^{7+} salt, $KMnO_4$ (Sigma Aldrich, ≥ 99% purity) was chosen. 5 mM manganese salt precursors concentration was used to synthesize free-standing nanoparticles. Meanwhile, higher salt concentration is required for carbon supported manganese oxide. Carbon powder (Vulcan XC-72, Cabot Carbon Corporation, USA) with a concentration of 2.2 g/L was used as support material and dispersed in the precursor solution by ultrasonic bath for 30 min before radiation.

In the oxidation route, the sample solution was purged with N_2O for 30 min to reach N_2O saturation in water (~2.5×10^{-2} M) at room temperature. In the reduction route, 1 M isopropanol was added to the sample solution and with N_2 gas purging for 30 min to remove oxygen from the solution.

The prepared samples were sealed and subjected for irradiation in a gamma-cell (MDS Norditon 1000 Elite Cs-137) with a dose rate of 0.124 Gy s^{-1}. After irradiation, the samples were filtered and washed with Milli-Q water. Thereafter, the samples containing carbon support were placed into a furnace, dried at 60 ℃ in air for 24 h.

The synthesis parameters for γ-radiation induced fabrication of manganese oxide particles both free-standing and on carbon support are summarized in Table 1.

The free-standing manganese oxides produced *via* reduction and oxidation routes are denoted as MnO_x-Red and MnO_x-Oxi, respectively, whereas, carbon black supported samples are denoted as MnO_x-Red/C and MnO_x-Oxi/C in Table 1.

A number of samples were synthesized. However we chose to describe four samples which are typical representatives of the MnO_x samples obtained *via* radiolytic reduction and oxidation routes. (see Table 1). The influence of other synthesis parameters, such as precursor types ($MnSO_4$, $MnCl_2$), concentration, total irradiation dose and solution pH (from 1.5 to 4.5), on MnO_x structure and its physical properties were studied. The results are shown in Supplementary Information. It was found that those parameters have less significant contribution to MnO_x properties alteration as compared to that caused by the changing redox conditions.

2.3. Characterization of structural and chemical composition

Powder X-ray diffraction (XRD) patterns of obtained samples were recorded by a PANalytical X'Pert PRO diffraction system with Cu Kα radiation (λ = 1.5418 Å) in a Bragg-Brentano geometry. The angular (2θ) range of 15° to 90° with a step of 0.01° was used.

The morphologies of the samples were investigated by transmission electron microscopy (TEM) operated at 200 kV using JEOL2100F and Hitachi S-4800 scanning electron microscope (SEM) at a voltage of 15 kV.

The mass loading (wt. %) of manganese on carbon was measured with ICP-OES (Inductively Coupled Plasma-Optical Emission Spectroscopy) method by a Thermo scientific iCAP 600 series instrument. Prior to ICP-OES measurements, 0.2 g of dry powder of each sample was immersed into 20 ml of 5% HNO_3 with high speed stirring for 24 h. The analysis of Mn was performed at wavelengths of 279 nm and 285.2 nm.

The oxidation states of Mn were analysed using X-ray photoelectron spectroscopy (XPS). For the MnO_x-Red samples, XPS spectra were recorded with a Kratos Axis Ultra electron spectrometer with a delay line detector. A monochromatic Al Kα source operated at 150 W and a charge neutralizer was used for the measurements. The chamber pressure was below 3×10^{-9} Torr. For the MnO_x-Oxi samples, XPS spectra were recorded with a PerkinElmer PHI 5000C ESCA system. A monochromatic Al Kα (1486.7 eV) source operated at 50 W and a charge neutralizer was used for the XPS measurements. The chamber pressure was kept below 6×10^{-10} Torr. The concentric hemispherical analyzer was positioned at a 45° angle with respect to the sample normal. The binding energy (BE) scale was referenced to the C 1 s of adventitious carbon, set at 284.8 eV. Processing of the spectra was accomplished with Kratos software using Gaussian and Lorenzian functions in the ratio of 70% to 30%. A Shirley background was applied. The element detection limit was typically 0.1 at%.

2.4. Electrochemical characterization.

Rotating disc electrode (RDE) measurements were performed to evaluate the ORR activity and carried out on mirror polished glassy carbon electrodes with a geometric area of 0.196 cm^2. The electrodes were modified by drop casting specific volumes of catalyst ink and then dried naturally in ambient environment. The details of the ink preparation and electrode modification were described in supplementary information.

All electrochemical measurements were performed in a three-electrode system using a potentiostat (Bio-Logic SP-300) with a graphite rod as a counter electrode and an Ag/AgCl in saturated KCl solution as a reference electrode. All the potentials reported here were iR-corrected (85% automatic iR compensation) and calibrated to reversible hydrogen electrode (RHE) according to E(RHE) = E(Ag/AgCl) + 0.964 V in 0.1 M KOH.

The electrochemical active surface area (ECSA) of the catalysts was estimated by double-layer capacitance (C_{dl}) measurements, according to the method reported in the literature [43]. The double layer charging current (i_c) was obtained from CVs at multiple scan rates (υ) at 0.4 V, which was in the potential region where the presence of faradaic currents was minimized and the total current dominated by capacitive currents. By plotting i_c as a function of υ, the slope of the linear fit was equal to C_{dl} ($i_c = \upsilon\, C_{dl}$). The ECSA of the catalyst was calculated by dividing C_{dl} by 0.040 mF cm^{-2}, a typical value reported for Mn electrode in alkaline aqueous solution [43,44]. It should be noted that the calculated ECSA only provides an approximate guide, and since the carbon support also contributes to the capacity, it will represent an overestimation. The electron transfer number (n) was calculated using the

Table 1
Radiation induced-synthesis parameters: precursor and scavenger type, total irradiation dose, mass loading of Mn on carbon.

Sample	Precursor	Scavenger	Total irradiation dose	Mn mass loading
MnO_x-Red	5 mM $KMnO_4$	1 M isopropanol	8.9 kGy	
MnO_x-Red/C	15.4 mM $KMnO_4$	1 M isopropanol	44.6 kGy	5.7 wt%
MnO_x-Oxi	5 mM $MnCl_2$ $4H_2O$	~2.5×10^{-2} M N_2O	8.9 kGy	
MnO_x-Oxi/C	18 mM $MnCl_2$ $4H_2O$	~2.5×10^{-2} M N_2O	44.6 kGy	21 wt%

Koutecky-Levich (K-L) equation. The detailed description is given in the supplementary information.

3. Results and discussions

3.1. Composition, structure, and morphology of manganese oxide catalysts

3.1.1. XPS studies

The elemental composition of the manganese oxide particles deposited on carbon was acquired by XPS. Mn 2p and 3 s spectra are shown in Fig. 1 and the corresponding binding energies are presented in Table 2. As shown in Fig. 1 (a) and Table 2, three binding energies for Mn $2p_{3/2}$ are distinguished in both samples. Those energies correspond to different oxidation states of manganese: Mn^{3+} [45], Mn^{2+} [45–47] and Mn^{4+} [42,45,48]. The ratio of O1s to Mn $2p_{3/2}$ of the two samples are close to 1.2, thus, MnO_2 can be one of the oxides present in both samples [49]. Other oxides, especially mixed valence oxides are more difficult to identify. For example, spinel Mn_3O_4, [$Mn^{2+}Mn_2^{3+}O_4^{2-}$] has a structure where Mn^{2+} ions are in tetrahedral and Mn^{3+} ions are in octahedral sites [50]. This crystal system can undergo spontaneous symmetry breaking that leads to several structures such as MnO-Mn_2O_3 (Mn^{2+} and Mn^{3+}) and even 2MnO-MnO_2 (Mn^{2+}, Mn^{4+}) with a weak interaction between different ion sites can exist for Mn_3O_4 compound [42]. As reported in the literature, the difference in binding energies of Mn $2p_{1/2}$ and Mn $2p_{3/2}$ levels in the XPS spectrum for mixed oxides can be larger than that for a simple oxide [51]. In our case the spin–orbit splitting between Mn $2p_{1/2}$ and Mn $2p_{3/2}$ levels is 11.6 eV and 11.3 eV for MnO_x-Oxi/C and MnO_x-Red/C, respectively, which matches to the values for Mn_3O_4 [42,49,51]. Therefore, we can assume that manganese oxides with a mixed valence states can be present in both the studied samples.

To further estimate the average Mn valence state in the obtained oxides, we consider binding energies of Mn 3 s core–shell. The 3 s line for the 3d transition metals has a splitting that depends on the number of 3d electrons [52]. Thus, one can determine the valence state of Mn ions considering the splitting magnitude of Mn 3 s line as shown in Fig. 2 (b). The measured splitting of Mn 3 s lines of 4.7 eV for both samples correspond to $Mn^{3.6+}$ [53].

As shown in Table 2, the surface atomic ratio of Mn species in MnO_x-Oxi/C is higher than that in MnO_x-Red/C. Moreover, the Mn^{3+}/Mn^{4+} ratio in MnO_x-Oxi/C and MnO_x-Red/C samples calculated from XPS spectra, is 2.01 and 1.56, respectively. Since, as shown in the literature, ORR activity of different types of manganese oxide is dependent on the amount of Mn^{3+} on the surface due to Jahn-Teller distortion effects and the ease oxidation to Mn^{4+}, the ratio of Mn^{3+}/Mn^{4+} may be considered as an important parameter for the evaluation of the catalytic efficiency of manganese compounds [54].

The XPS studies demonstrate that the materials produced by γ-radiation induced synthesis *via* both oxidation and reducing routes consist of a mixture of solid manganese oxides having Mn ions in a 2+, 3 + and 4 + oxidation state.

3.1.2. XRD and electron microscopy studies

XRD and electron microscopy studies were performed to further elucidate the composition and structure of the synthesized material. XRD patterns for manganese oxide particles synthesized *via* oxidization and reduction routes are presented in Fig. 2 (a) and (c), respectively. The patterns were recorded from both free-standing and carbon supported particles.

The XRD patterns for the manganese oxide obtained by radiolytic oxidation are shown in Fig. 2 (a). The peaks denoted with Miller indices correspond to γ-MnO_2 phase (JCPDS 14–0644) [16,55]. This phase is constructed of [MnO_6] octahedral units, arranged in (1 × 2) and (1 × 1) tunnels [9]. As reported in the literature [16,55], the metastable γ-MnO_2 can transform to α-MnO_2 *via* increasing the reaction temperature or altering solution pH. As also seen in Fig. 1(a) the diffraction peak from carbon (at 2θ of about 25°) is almost negligible. This is probably due to the fact that Mn mass loading in MnO_x-Oxi/C sample is rather high (21 wt%), therefore, the intensity of diffraction peaks from amorphous carbon is dampened by the signal from MnO_x.

The morphology of γ-MnO_2 particles studied using SEM is shown in Fig. 2(b). As shown in the figure, the particles have a spherical shape composed of nanoflakes and possess a well-developed surface. The complex morphology of the obtained manganese oxide particles may indicate that their formation in solutions occurred *via* a non-classical crystallization pathway, when the crystallization occurs *via* the formation of a sequence of phases, from emulsion *via* amorphous phases to crystalline intermediates [56,57]. Although the XRD study indicates γ-MnO_2 is the only phase that formed during radiolytic oxidation, the XPS measurements reveal that Mn^{2+} and Mn^{3+} are also present in the samples. Hence, we assume γ-MnO_2 is a bulk crystalline phase, and meanwhile, contains amorphous phases of both Mn^{2+} and Mn^{3+} to be formed on the surface.

The manganese oxides synthesized by radiolytic reduction possess quite different structure and morphology as compared to that synthesized by radiolytic oxidation. As seen in Fig. 2(c), the XRD patterns for MnO_x-Red consist of the peaks, which belong to the tetragonal spinel-type Mn_3O_4 phase (JPCDS 24–0734) [44,58]. Essentially, these peaks belong to spinel which occurs in nature as the mineral hausmannite, where manganese exists in two oxidation states Mn^{2+} and Mn^{3+} (MnO-Mn_2O_3). However, as shown in the literature, another distorted structure of Mn_3O_4,

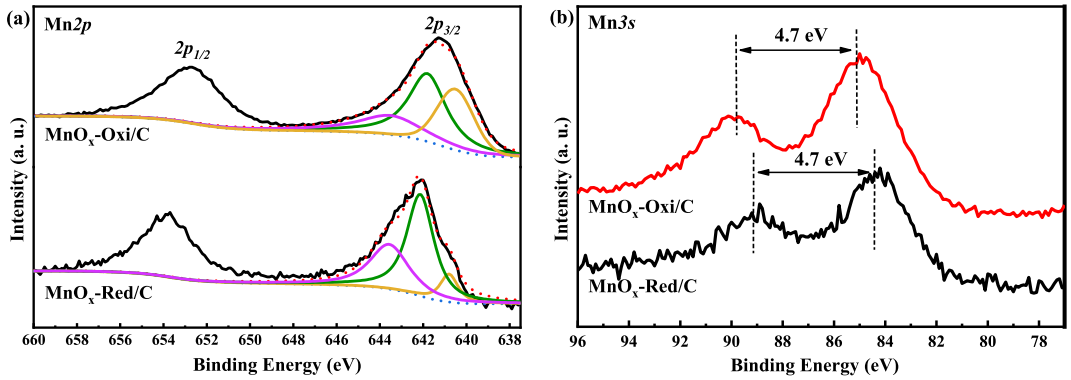

Fig. 1. Mn 2p (a) and Mn 3s (b) XPS spectra of carbon supported manganese oxide particles synthesized by both radiolytic oxidation (upper curves) and radiolytic reduction (lower curves) routes.

Table 2
Results of XPS studies of carbon supported manganese oxides synthesized by both radiolytic oxidation and radiolytic reduction.

	MnO_x-Oxi/C		MnO_x-Red/C	
Line (compound)	Binding Energy (eV)	Atomic ratio (at. %)	Binding Energy (eV)	Atomic ratio (at. %)
C 1 s (C—C)	284.8	81.45	284.3	92.53
O 1 s (Mn-O)	529.1	6.9	529.8	2.3
O 1 s (C═O, Mn-OH)	530.8	3.45	531.1	0.8
O 1 s (C—OH)	532.5	1.85	532.1	1.1
O 1 s (C—OH)			533.3	0.75
O 1 s (H_2O)			535.1	0.28
Mn $2p_{3/2}$ (Mn^{3+})	641.9	2.98	642.1	0.78
Mn $2p_{3/2}$ (Mn^{2+})	640.5	1.89	640.8	0.14
Mn $2p_{3/2}$ (Mn^{4+})	643.5	1.48	643.6	0.49
Mn $2p_{1/2}$	652.7		652.0	

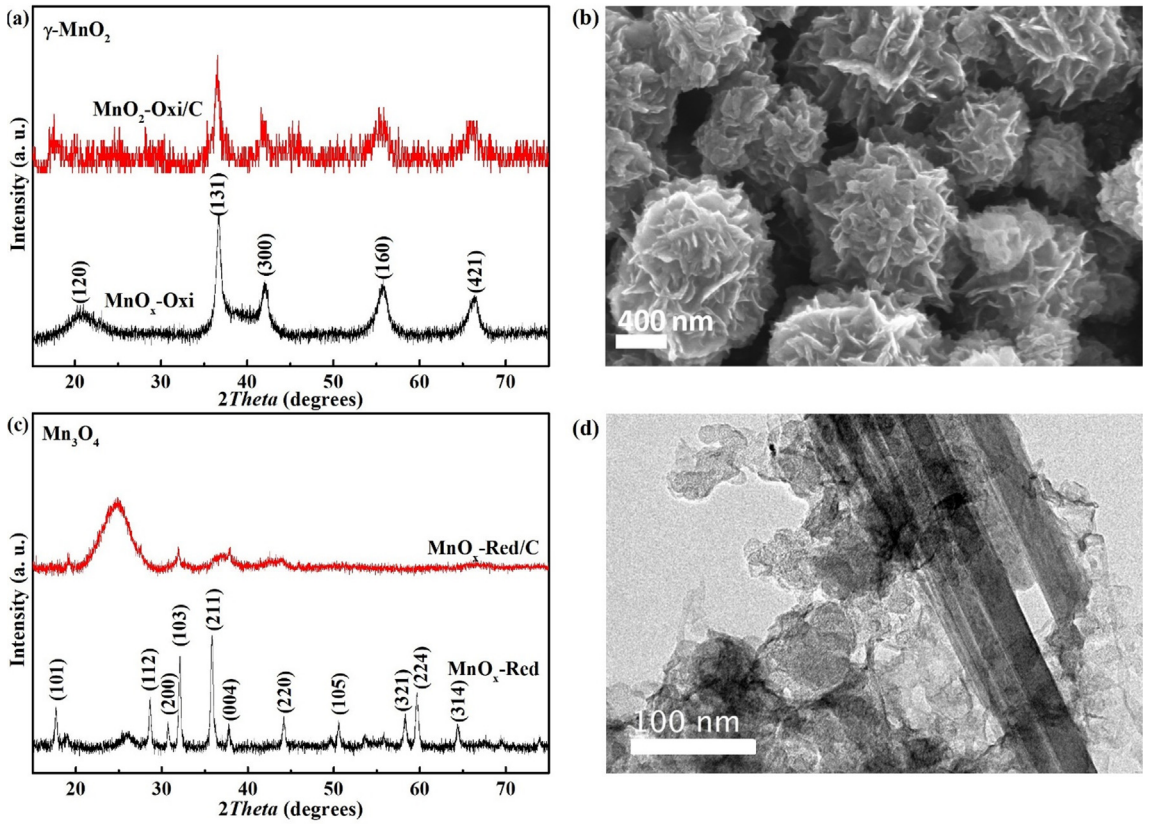

Fig. 2. X-ray diffraction patterns of free-standing manganese oxide particles and on a Vulcan X-72 synthesized by radiolytic oxidation (a); and radiolytic reduction (c). The wide XRD peaks at $2\theta \sim 25°$ correspond to amorphous carbon; SEM image of manganese oxide particles synthesized by radiolytic oxidation (b); TEM image of manganese oxide nano-rods synthesized by radiolytic reduction (d).

$2MnO\text{-}MnO_2$ with Mn^{2+} and Mn^{4+} can coexist [42]. Considering the results from the XPS study that shows the presence of Mn^{4+} together with Mn^{2+} (Mn^{3+}) at the surface, we expect that the composition of the samples obtained by the reduction route would rather correspond to $2MnO\text{-}MnO_2$ than to $MnO\text{-}Mn_2O_3$.

The morphology and the surface structure of the catalyst produced *via* the reduction route were characterized using TEM and shown in Fig. 2(d). Apart from the samples obtained by radiolytic oxidation, the sample synthesized *via* the reduction route consists of a mixture of nano-rods and nanowires. The amorphous carbon with "onion" structure is clearly seen in the image.

3.2. Electrochemical characterization

3.2.1. Electrocatalytic activity measured by RDE

The ORR measurements were performed in 0.1 M KOH with a rotating disk electrode (RDE) setup. Cyclic voltammetry (CV) of synthesized carbon supported manganese oxide catalysts and commercial Pt/C (20 wt%, ETEK) were obtained at a scan rate of 50 mV s^{-1} (Fig. 3(a)). The CV curves of MnO_x-Red/C and MnO_x-Oxi/C samples showed reduction peaks at potentials around 0.7 V and oxidation peaks around 1.05 V, which was consistent with the result in literature [59]. Pt/C showed the standard CV curve with characteristic shape of polycrystalline Pt in alkaline medium [60]. The ORR kinetics of the carbon supported manganese oxide catalysts was investigated by collecting polarization curves at various rotation speeds (Fig. 3(b) and (c)). For all the samples, the higher rotation speed will give faster oxygen diffusion, thus resulting in higher diffusion limiting current density (J_d). Table 3 summarizes the key parameters for ORR performance obtained from the polarization curves. It can be seen that, the J_d of MnO_x-Oxi/C almost reached the value of Pt/C (5.0 mA cm^{-2}) and much higher than that of MnO_x-Red/C (2.8 mA cm^{-2}). Both of the onset potential E_{onset} and half-wave potential $E_{1/2}$ of synthesized carbon supported

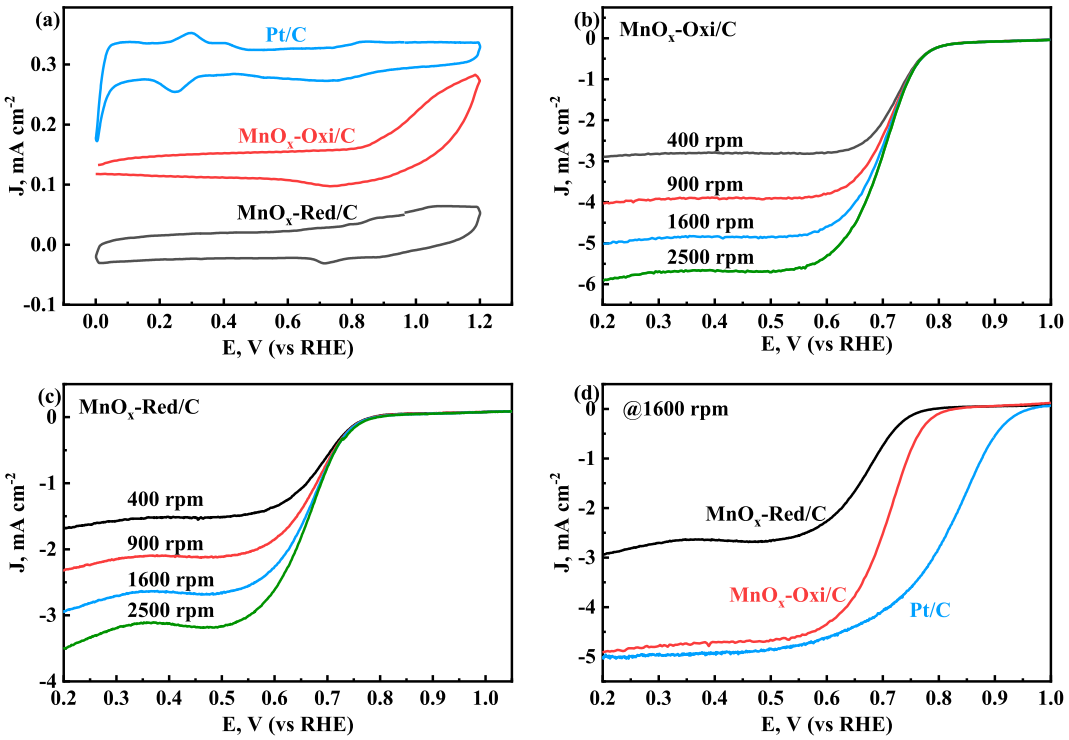

Fig. 3. Cyclic Voltammetry curves recorded for MnO_x-Oxi/C, MnO_x-Red/C and commercial Pt/C (20%) catalysts in N_2 saturated 0.1 M KOH solution with the scan rate at 50 mV s^{-1}(a). Polarization curves at different rotation rates measured on manganese oxide catalysts synthesized by oxidation (b) and reduction (c) routes. Polarization curves of MnO_x-Oxi/C, MnO_x-Red/C and Pt/C at the rotation speed of 1600 rpm (d). All the polarization curves in Fig. 3(b)–(d) were recorded at the scan rate of 10 mV s^{-1}. (For interpretation of the references to colour in this figure legend, the reader is referred to the web version of this article.)

Table 3
ORR performance parameters obtained from polarization curves shown in Fig. 3(d). Electron transfer number was calculated from K-L plots in Fig. 4 (a).

Sample	J_d ($mAcm^{-2}$)	Electron transfer number	E_{onset} (V)	$E_{1/2}$ (V)	Specific Activity @ 0.7 V (mA cm^{-2})
MnO_x-Oxi/C	4.8	4.1	0.8	0.71	0.03
MnO_x-Red/C	2.8	2.6	0.76	0.66	0.02
Pt/C	5	4.0	0.94	0.82	0.91

manganese oxide catalysts were lower than Pt/C, but it can be clearly seen that the potentials of MnO_x-Oxi/C were much more positive than that of MnO_x-Red/C, which indicates a higher ORR activity of the MnO_x-Oxi/C sample at low overpotentials. The $E_{1/2}$ of Pt/C sample showed a little negative shift comparing with the value in some other studies but it should be noted that all the ORR parameters of Pt/C were within the range that have been reported in literatures where the similar recipe of catalyst ink and conditions of measurement were applied [61–63]. To investigate the first order ORR kinetics, the electron transfer number (n) was determined by K-L plots ((Fig. 4(a)). The calculated electron transfer number of MnO_x-Red/C sample was 2.6, whereas, the n value for MnO_x-Oxi/C and Pt/C were 4.0 and 4.1, respectively, demonstrating a four-electron oxygen reduction pathway and the high electro-catalytic activity towards ORR. This matches very well with the fact that the diffusion limited current of sample MnO_x-Red/C was about half of sample MnO_x-Oxi/C.

To eliminate the effect of a carbon support, the ORR activity for both MnO_x-Oxi/C and MnO_x-Red/C catalysts having similar Mn loading, was investigated. Therefore, a MnO_x-Red/C sample that contains 21 wt% of Mn was prepared, and its ORR activity was compared to the activity of the other samples. The results are shown in Fig. S3. As seen in the figure the overall ORR activity of MnO_x-red/C catalysts only slightly increases when concentration of Mn in the sample is increased by 3.7 times (from 5.7 wt% to 21 wt%). Still this activity remains significantly smaller than the ORR activity of a MnOx-Oxi/C sample. Dissimilarity in the samples' morphology, nano-rods and hollow spheres in MnO_x-red/C and MnOx-Oxi/C samples, respectively, can be a possible reason for the difference in the electrochemical performance of the MnOx catalysts

3.2.2. Electrochemical active surface area of the MnO_x/C catalysts

The electrochemical active surface area (ECSA) measurement provides information on the number of electrochemically active sites on the electrode which directly relates to the sample's electrocatalytic activity [64,65]. In the current work, the ECSA of the catalysts was estimated by analysing the double-layer capacitance and the actual amount of metal on GC electrode which was determined by ICP-OES after electrochemical test. Fig. 4(b) shows the plot of capacitive currents as a function of the scan rate with the corresponding linear fits. The capacitive currents were obtained from the CVs in the non-Faraday region, which are presented in Fig. S1. Table S1 lists the double-layer capacitance (C_{dl}) and ECSA value of MnO_x-Oxi/C and MnO_x-Red/C samples, respectively. The ECSA of sample MnO_x-Oxi/C (113.9 m^2 g_{Mn}^{-1}) is twice as large as that of MnO_x-Red/C (52.3 m^2 g_{Mn}^{-1}), which can be attributed to the high porosity and large surface area, mainly owing to the accumulation of nanoflakes on its surface and, thus, results in an overall

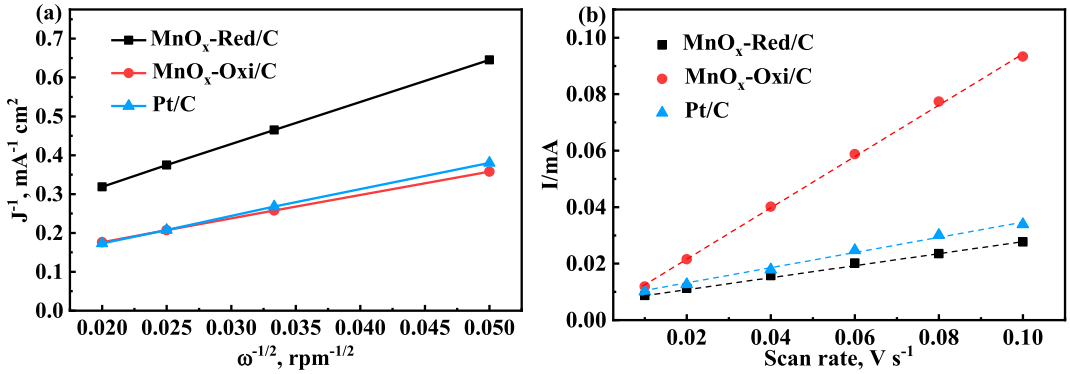

Fig. 4. K – L plots calculated for MnO_x-Oxi/C, MnO_x-Red/C and commercial Pt/C electrodes at 0.4 V (*vs* RHE), ***J*** is a current density, ***ω*** is a rotation rate of a disk electrode (a). Capacitive current as a function of the scan rate with corresponding linear fits to the experimental data (b). (For interpretation of the references to colour in this figure legend, the reader is referred to the web version of this article.)

three-dimensional hierarchical nanostructure. The ECSA of Pt/C calculated from C_{dl} is 171.2 m^2/g_{Pt}, which is larger than what has been previously reported [66,67], indicating the fact that the double-layer capacitance method may not be a suitable technique to determine the ECSA of Pt/C sample. Therefore, the ECSA was recalculated at 43.1 m^2/g_{Pt} based on the modified H_{upd} method [68], and the value is within the range reported in literatures [62,63,66]. Specific activity of the catalysts has been calculated from the ECSA and listed in Table 3. As seen in the table the specific activity of both MnO_x/C samples is much lower than that of Pt/C, which is expected. However, MnO_x-Oxi/C sample showed higher specific activity than MnO_x-Red/C, which could be ascribed to the difference in samples morphology and composition. The way to improve the specific activity of manganese based catalysts can include reducing the size of the active compounds down to a level of a single atom, as well as using different supports such as, for example, nitrogen-doped carbon, to create active interfacial sites [69,70]. Although this is beyond the scope of the current study, it can be a topic for future investigations.

The results of stability tests performed on both types of catalysts in O_2 saturated 0.1 M KOH solution are shown in Fig. 5. As seen in the figure both MnO_x/C samples exhibited good electrochemical stability. The current density of MnO_x-Oxi/C showed a decrease from the initial value 1.48 mA cm^{-2} to 1.40 mA cm^{-2} after 10000 s of the experiment run at 0.7 V (5.4% decay). Also, the current density of MnO_x-Red/C had a minor increase (from 0.30 mA cm^{-2} in initial to 0.41 after 5000 s) followed by a small decrease (ended at 0.38 mA cm^{-2} after 10000 s). Good stability of MnO_x/C samples may be attributed to the special morphology of the catalyst which can keep the overall structure and composition from further transformation, and thus, the active sites could be then maintained to a great extent. Small fluctuations of current density in MnO_x-Red/C sample could be due to possible de-adhesion of the neighbor nanorods, thus exposing more active sites and resulting in increasing current density.

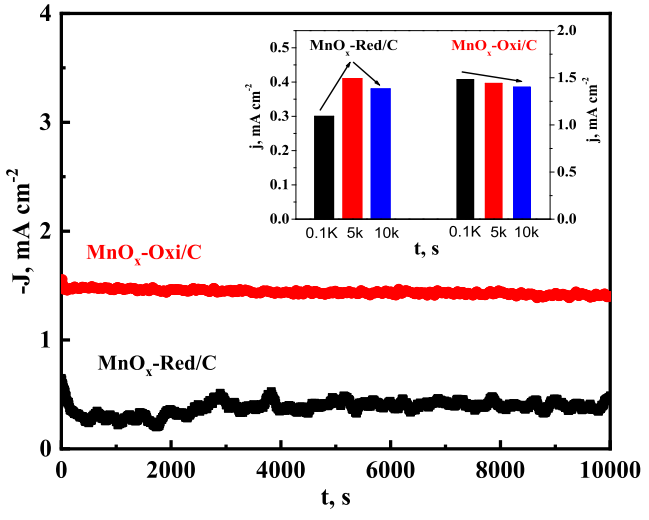

Fig. 5. Stability test of MnO_x-Oxi/C and MnO_x-Red/C carried out by chronoamperometry method in O_2 saturated 0.1 M KOH solution with fixed potential at 0.7 V (*vs* RHE) for 10000 s, ***J*** is a current density, ***t*** is test time. Inset is the current density measured after 100 s, 5000 s and 10000 s of the experiment run. (For interpretation of the references to colour in this figure legend, the reader is referred to the web version of this article.)

4. Conclusions

In this study we demonstrated that by varying redox condition of a precursor solution in the γ-radiation induced synthesis one can tune the morphology, composition and electrochemical performance of manganese oxide catalysts. Manganese oxide nanoparticles both free standing and on carbon support were synthesized by γ-radiation induced synthesis method. Both radiolytic oxidation and reduction were used. The samples prepared *via* the oxidation route possess a hollow spherical shape composed of nanoflakes, which structure corresponds to that of γ-MnO_2. Meanwhile, the samples produced *via* the reduction route possess a rod-like morphology and have Mn_3O_4 (probably 2MnO-MnO_2) as the main crystalline phase. The ORR activities of the obtained catalysts were controlled by RDE measurements. It was found that samples synthesized via radiolytic oxidation exhibit a 4-electron pathway, while an indirect 2-electron pathway was observed in the samples obtained via radiolytic reduction. High ORR activity of the MnO_x-Oxi/C sample can be attributed to its high electrochemical surface area originating from the three-dimensional hierarchical nanostructure. Moreover, as confirmed by the XPS analysis, the surface concentration of Mn^{3+} in the MnO_x-Oxi/C sample is larger than that in the MnO_x-Red/C sample, which may contribute to the increased electro-catalytic activity of the former. In addition, both types of catalysts demonstrated good electrochemical stability in alkaline solutions. Thus, the γ-radiation induced synthesis method can be applied as a structural and composition adjustable approach to fabricate manganese oxide electro-catalyst with improved ORR activity and stability.

CRediT authorship contribution statement

Z. Li: Data curation, formal analysis, Investigation, Writing original draft, Writing review and editing. **Y. Yang:** Data curation, formal analysis, Investigation, Writing original draft. **A. Relefors:** Data curation, formal analysis, Investigation. **X. Kong:** Data curation,

formal analysis, Investigation. **G. M. Siso:** Data curation, formal analysis, Investigation. **I. L. Soroka:** Data curation, formal analysis, Supervision, Investigation, Writing original draft, Writing review and editing. **B. Wickman:** Supervision, Investigation. **Y. Kiros:** Supervision, Investigation.

Declaration of Competing Interest

The authors declare that they have no known competing financial interests or personal relationships that could have appeared to influence the work reported in this paper.

Acknowledgements

The authors acknowledge Swedish Foundation for Strategic Research (SSF) and 2019 Shanghai Jiao Tong University- KTH Royal Institute of Technology(SJTU-KTH) strategic partnership foundation for the financial support of the current study. Z. L acknowledge the China Scholarship Council (Grant Number: 201700260193). B. W. thank the Swedish Research Council (Project No. 2018- 03927). I. L. S acknowledge A. Shchukarev for XPS measurements and also C. Taylor, M. Goy, C. Kihlblom, F. Boström for the contribution to the particles synthesis and characterization.

Appendix A. Supplementary material

Supplementary data to this article can be found online at https://doi.org/10.1016/j.jcis.2020.09.011.

References

[1] T. Najam, X. Cai, M.K. Aslam, M.K. Tufail, S.S.A. Shah, Nano-engineered directed growth of Mn_3O_4 quasi-nanocubes on N-doped polyhedrons: Efficient electrocatalyst for oxygen reduction reaction, Int. J. Hydrogen Energy 45 (23) (2020) 12903–12910, https://doi.org/10.1016/j.ijhydene.2020.02.205.

[2] Y. Makimura, T. Ohzuku, Lithium insertion material of $LiNi_{1/2}Mn_{1/2}O_2$ for advanced lithium-ion batteries, J. Power Sour. 119–121 (2003) 156–160, https://doi.org/10.1016/S0378-7753(03)00170-8.

[3] M.M. Thackeray, Manganese oxides for lithium batteries, Prog. Solid State Chem. 25 (1–2) (1997) 1–71, https://doi.org/10.1016/S0079-6786(97)81003-5.

[4] D. Guo, S. Dou, X. Li, J. Xu, S. Wang, L. Lai, et al., Hierarchical MnO_2/rGO hybrid nanosheets as an efficient electrocatalyst for the oxygen reduction reaction, Int. J. Hydrogen Energy 41 (10) (2016) 5260–5268, https://doi.org/10.1016/j.ijhydene.2016.01.070.

[5] F. Cheng, Y. Su, J. Liang, Z. Tao, J. Chen, MnO_2-based nanostructures as catalysts for electrochemical oxygen reduction in alkaline media, Chem. Mater. 22 (22) (2010) 898–905, https://doi.org/10.1021/cm901698s.

[6] H. Zheng, M. Modibedi, M. Mathe, K. Ozoemena, The thermal effect on the catalytic activity of MnO_2 (α, β, and γ) for oxygen reduction reaction, Mater. Today:. Proc. 4 (11) (2017) 11624–11629, https://doi.org/10.1016/j.matpr.2017.09.074.

[7] N. Ominde, N. Bartlett, X.Q. Yang, D. Qu, Investigation of the oxygen reduction reaction on the carbon electrodes loaded with MnO_2 catalyst, J. Power Sour. 195 (13) (2010) 3984–3989, https://doi.org/10.1016/j.jpowsour.2009.12.128.

[8] J.P. Brenet, Electrochemical behaviour of metallic oxides, J. Power Sour. 4 (3) (1979) 183–190, https://doi.org/10.1016/0378-7753(79)85009-0.

[9] J.E. Post, Manganese oxide minerals: Crystal structures and economic and environmental significance, PNAS 96 (7) (1999) 3447–3454, https://doi.org/10.1073/pnas.96.7.3447.

[10] S.L. Brock, N. Duan, Z.R. Tian, O. Giraldo, H. Zhou, S.L. Suib, A Review of Porous Manganese Oxide Materials, Chem. Mater. 10 (10) (1998) 2619–2628, https://doi.org/10.1021/cm980227h.

[11] X. Wang, Y. Li, Selected-control hydrothermal synthesis of α- and β-MnO_2 single crystal nanowires, J. Am. Chem. Soc. 124 (12) (2002) 2880–2881, https://doi.org/10.1021/ja0177105.

[12] X. Huang, D. Lv, H. Yue, A. Attia, Y. Yang, Controllable synthesis of α- and β-MnO_2: Cationic effect on hydrothermal crystallization, Nanotechnology 19 (22) (2008) 225606, https://doi.org/10.1088/0957-4484/19/22/225606.

[13] X. Shi, S. Ahmad, K. Pérez-Salcedo, B. Escobar, H. Zheng, A.M. Kannan, Maximization of quadruple phase boundary for alkaline membrane fuel cell using non-stoichiometric α-MnO_2 as cathode catalyst, Int. J. Hydrogen Energy 44 (2) (2019) 1166–1173, https://doi.org/10.1016/j.ijhydene.2018.11.042.

[14] Y.L. Cao, H.X. Yang, X.P. Ai, L.F. Xiao, The mechanism of oxygen reduction on MnO_2-catalyzed air cathode in alkaline solution, J. Electroanal. Chem. 557 (15) (2003) 127–134, https://doi.org/10.1016/S0022-0728(03)00355-3.

[15] P.C. Li, C.C. Hu, T.C. Lee, W.S. Chang, T.H. Wang, Synthesis and characterization of carbon black/manganese oxide air cathodes for zinc-air batteries, J. Power Sources 269 (10) (2014) 88–97, https://doi.org/10.1016/j.jpowsour.2014.06.108.

[16] J. Yang, J. Wang, S. Ma, B. Ke, L. Yu, W. Zeng, et al., Insight into the effect of crystalline structure on the oxygen reduction reaction activities of one-dimensional MnO_2, Phys E Low-Dimensional Syst. Nanostruct. 109 (2019) 191–197, https://doi.org/10.1016/j.physe.2018.07.032.

[17] J.R. Goldstein, A.C.C. Tseung, A Joint pseudo-splitting/peroxide mechanism for oxygen reduction at fuel cell cathodes, Nature 222 (5196) (1969) 869–870, https://doi.org/10.1038/222869a0.

[18] X. Li, X. Ma, D. Su, L. Liu, R. Chisnell, S.P. Ong, et al., Direct visualization of the Jahn-Teller effect coupled to Na ordering in $Na_{5/8}MnO_2$, Nat. Mater. 13 (6) (2014) 586–592, https://doi.org/10.1038/nmat3964.

[19] F.H.B. Lima, M.L. Calegaro, E.A. Ticianelli, Investigations of the catalytic properties of manganese oxides for the oxygen reduction reaction in alkaline media, J. Electroanal. Chem. 590 (2) (2006) 152–160, https://doi.org/10.1016/j.jelechem.2006.02.029.

[20] Y. Kiros, S. Schwartz, Pyrolyzed macrocycles on high surface area carbons for the reduction of oxygen in alkaline fuel cells, J. Power Sour. 36 (4) (1991) 547–555, https://doi.org/10.1016/0378-7753(91)80080-H.

[21] A.L. Dicks, The role of carbon in fuel cells, J. Power Sour. 156 (2) (2006) 128–141, https://doi.org/10.1016/j.jpowsour.2006.02.054.

[22] H. Wang, H. Dai, Strongly coupled inorganic–nano-carbon hybrid materials for energy storage, Chem. Soc. Rev. 42 (7) (2013) 3088–3113, https://doi.org/10.1039/c2cs35307e.

[23] N. Mackiewicz, G. Surendran, H. Remita, B. Keita, G. Zhang, L. Nadjo, et al., Supramolecular self-assembly of amphiphiles on carbon nanotubes: A versatile strategy for the construction of CNT/metal nanohybrids, application to electrocatalysis, J. Am. Chem. Soc. 130 (26) (2008) 8110–8111, https://doi.org/10.1021/ja8026373.

[24] I. Roche, E. Chaînet, M. Chatenet, J. Vondrák, Carbon-supported manganese oxide nanoparticles as electrocatalysts for the Oxygen Reduction Reaction (ORR) in alkaline medium: Physical characterizations and ORR mechanism, J. Phys. Chem. C 111 (3) (2007) 1434–1443, https://doi.org/10.1021/jp0647986.

[25] R.N. Reddy, R.G. Reddy, Sol-gel MnO_2 as an electrode material for electrochemical capacitors, J. Power Sour. 124 (1) (2003) 330–337, https://doi.org/10.1016/S0378-7753(03)00600-1.

[26] H. Zheng, J. Wang, Y. Jia, C. Ma, In-situ synthetize multi-walled carbon nanotubes@MnO_2 nanoflake core-shell structured materials for supercapacitors, J. Power Sour. 216 (15) (2012) 508–514, https://doi.org/10.1016/j.jpowsour.2012.06.047.

[27] F. Cheng, J. Zhao, W. Song, C. Li, H. Ma, J. Chen, et al., Facile controlled synthesis of MnO_2 nanostructures of novel shapes and their application in batteries, Inorg. Chem. 45 (5) (2006) 2038–2044, https://doi.org/10.1021/ic051715b.

[28] T. Cetinkaya, H. Akbulut, M. Tokur, S. Ozcan, M. Uysal, High capacity Graphene/α-MnO_2 nanocomposite cathodes for Li–O_2 batteries, Int. J. Hydrogen Energy 41 (23) (2016) 9746–9754, https://doi.org/10.1016/j.ijhydene.2016.02.093.

[29] Y.U. Jeong, A. Manthiram, Nanocrystalline Manganese Oxides for Electrochemical Capacitors with Neutral Electrolytes, J. Electrochem. Soc. 149 (11) (2002) A1419, https://doi.org/10.1149/1.1511188.

[30] Y. Liu, Y. Qian, Y. Zhang, M. Zhang, Z. Chen, L. Yang, et al., Preparation of nanocrystalline manganic oxide Mn_2O_3 powders by use of γ-ray radiation, Mater. Lett. 28 (4–6) (1996) 357–359, https://doi.org/10.1016/0167-577X(96)00086-9.

[31] Y.P. Liu, Y.T. Qian, Y.H. Zhang, M.W. Zhang, C.S.LY. Wang, γ-ray radiation preparation and characterization of nanocrystalline manganese dioxide, Mater Res Bull 32 (8) (1997) 1055–1062. https://doi.org/10.1016/S0025-5408(97)00069-X.

[32] R. Puspalata, S. Sumathi, P. Chandramohan, S. Bera, S. Rangarajan, R. Sudha, et al., Gamma radiation induced formation and characterization of the nano-oxides of manganese, Radiat. Phys. Chem. 85 (2013) 152–160, https://doi.org/10.1016/j.radphyschem.2012.12.018.

[33] A.J. Berejka, Irradiation processing in the '90's: energy savings and environmental benefits, Radiat. Phys. Chem. 46 (4) (1995) 429–437, https://doi.org/10.1016/0969-806X(95)00188-4.

[34] P. Yadav, R.T. Olsson, M. Jonsson, Synthesis and characterization of MnO_2 colloids, Radiat. Phys. Chem. 78 (11) (2009) 939–944, https://doi.org/10.1016/j.radphyschem.2009.02.006.

[35] C. Lume-Pereira, S. Baral, A. Henglein, E. Janata, Chemistry of colloidal manganese dioxide. 1. Mechanism of reduction by an organic radical (a radiation chemical study), J. Phys. Chem. 89 (26) (1985) 5772–5778, https://doi.org/10.1021/j100272a040.

[36] S. Baral, C. Lume-Pereira, E. Janata, A. Henglein, Chemistry of colloidal manganese oxides. 3. Formation in the reaction of hydroxyl radicals with Mn^{2+} ions, J. Phys. Chem. 90 (22) (1986) 6025–6028, https://doi.org/10.1021/j100280a113.

[37] A.J. Swallow, An introduction to radiation chemistry, Int. J. Radiat Biol. 30 (4) (1976), https://doi.org/10.1080/09553007614551181. 399-399.

[38] H.A. Schwarz, Free radicals generated by radiolysis of aqueous solutions, J. Chem. Educ. 58 (2) (1981) 101–105, https://doi.org/10.1021/ed058p101.

[39] H.A. Schwarz, R.W. Dodson, Equilibrium between hydroxyl radicals and thallium(II) and the oxidation potential of OH(aq), J. Phys. Chem. 88 (16) (1984) 3643–3647, https://doi.org/10.1021/j150660a053.

[40] P. Wardman, Reduction Potentials of One Electron Couples Involving Free Radicals in Aqueous Solution, J. Phys. Chem. Ref. Data 18 (4) (1989) 1637–1755, https://doi.org/10.1063/1.555843.
[41] J. Hem, Chemical equilibria and rates of manganese oxidation - Chemistry of Manganese in Natural Water, UNITED STATES GOVERNMENT PRINTING OFFICE, WASHINGTON, 1963.
[42] A. Moses Ezhil Raj, S.G. Victoria, V.B. Jothy, C. Ravidhas, J. Wollschläger, M. Suendorf, M. Neumann, M. Jayachandran, C. Sanjeeviraja, XRD and XPS characterization of mixed valence Mn_3O_4 hausmannite thin films prepared by chemical spray pyrolysis technique, Appl. Surf. Sci. 256 (9) (2010) 2920–2926, https://doi.org/10.1016/j.apsusc.2009.11.051.
[43] C.C.L. McCrory, S. Jung, J.C. Peters, T.F. Jaramillo, Benchmarking heterogeneous electrocatalysts for the oxygen evolution reaction, J. Am. Chem. Soc. 135 (45) (2013) 16977–16987, https://doi.org/10.1021/ja407115p.
[44] T. Li, B. Xue, B. Wang, G. Guo, D. Han, Y. Yan, et al., Tubular Monolayer Superlattices of Hollow Mn_3O_4 Nanocrystals and Their Oxygen Reduction Activity, J. Am. Chem. Soc. 139 (35) (2017) 12133–12136, https://doi.org/10.1021/jacs.7b06587.
[45] D. Chinnadurai, M. Nallal, H.J. Kim, O.L. Li, K.H. Park, K. Prabakar, Mn^{3+} Active Surface Site Enriched Manganese Phosphate Nano-polyhedrons for Enhanced Bifunctional Oxygen Electrocatalyst, ChemCatChem 12 (8) (2020) 2348–2355, https://doi.org/10.1002/cctc.202000164.
[46] C.D. Wagner, W.M. Riggs, L.E. Davis, J.F. Moulder GEM, Handbook of X-ray photoelectron spectroscopy, Perkin-Elmer Corporation (1979), https://doi.org/10.1002/sia.740030412.
[47] M. Oku, K. Hirokawa, X-ray photoelectron spectroscopy of Co_3O_4, Fe_3O_4, Mn_3O_4, and related compounds, J. Electron Spectros. Relat. Phenomena 8 (5) (1976) 475–481, https://doi.org/10.1016/0368-2048(76)80034-5.
[48] M. Oku, K. Hirokawa, S. Ikeda, X-ray photoelectron spectroscopy of manganese-oxygen systems, J. Electron Spectros. Relat. Phenomena 7 (5) (1975) 465–473, https://doi.org/10.1016/0368-2048(75)85010-9.
[49] J.S. Foord, R.B. Jackman, G.C. Allen, An X-ray photoelectron spectroscopic investigation of the oxidation of manganese, Philos. Mag. A Phys. Condens. Matter. Struct. Defects. Mech. Prop. 49 (5) (1984) 657–663, https://doi.org/10.1080/01418618408233293.
[50] K. Satomi, Oxygen Positions Parameters of Tetragonal Mn_3O_4, J. Phys. Soc. Japan 16 (1961) 258–266, https://doi.org/10.1143/JPSJ.16.258.
[51] Y. Jian, M. Ma, C. Chen, C. Liu, Y. Yu, Z. Hao, et al., Tuning the micromorphology and exposed facets of MnO_x promotes methyl ethyl ketone low-temperature abatement: Boosting oxygen activation and electron transmission, Catal. Sci. Technol. 8 (15) (2018) 3863–3875, https://doi.org/10.1039/c8cy00444g.
[52] V.A.M. Brabers, F.M. van Setten, P.S.A. Knapen, X-ray photoelectron spectroscopy study of the cation valencies in nickel manganite, J. Solid State Chem. 49 (1) (1983) 93–98, https://doi.org/10.1016/0022-4596(83)90220-7.
[53] Q.H. Wu, J.M. Xu, Q.C. Zhuang, S.G. Sun, X-ray photoelectron spectroscopy of $LiM_{0.05}Mn_{1.95}O_4$ (M = Ni, Fe and Ti), Solid State Ionics 177 (17–18) (2006) 1483–1488, https://doi.org/10.1016/j.ssi.2006.06.020.
[54] B. Zhang, H. Chen, Q. Daniel, B. Philippe, F. Yu, M. Valvo, et al., Defective and "c-Disordered" Hortensia-like Layered MnO_x as an Efficient Electrocatalyst for Water Oxidation at Neutral pH, ACS Catal. 7 (9) (2017) 6311–6322, https://doi.org/10.1021/acscatal.7b00420.
[55] Y. Khan, S.K. Durrani, M. Mehmood, M.R. Khan, Mild hydrothermal synthesis of γ-MnO_2 nanostructures and their phase transformation to α-MnO_2 nanowires, J. Mater. Res. 26 (17) (2011) 2268–2275, https://doi.org/10.1557/jmr.2011.138.
[56] I.L. Soroka, K.K. Norrfors, N.V. Tarakina, Nonconvex Morphology of Metallic Copper Obtained via Nonclassical Crystallization of Copper Hydride, Cryst. Growth Des. 19 (9) (2019) 5275–5282, https://doi.org/10.1021/acs.cgd.9b00689.
[57] H. Cölfen, M. Antonietti, Mesocrystals: Inorganic superstructures made by highly parallel crystallization and controlled alignment, Angew Chem. – Int. Ed. 44 (35) (2005) 5576–5591, https://doi.org/10.1002/anie.200500496.
[58] C.C. Hu, C.Y. Hung, K.H. Chang, Y.L. Yang, A hierarchical nanostructure consisting of amorphous MnO_2, Mn_3O_4 nanocrystallites, and single-crystalline MnOOH nanowires for supercapacitors, J. Power Sour. 196 (2) (2011) 847–850, https://doi.org/10.1016/j.jpowsour.2010.08.001.
[59] S. Cao, N. Han, J. Han, Y. Hu, L. Fan, C. Zhou, et al., Mesoporous Hybrid Shells of Carbonized Polyaniline/Mn_2O_3 as Non-Precious Efficient Oxygen Reduction Reaction Catalyst, ACS Appl. Mater. Interf. 8 (9) (2016) 6040–6050, https://doi.org/10.1021/acsami.5b11955.
[60] P. Daubinger, J. Kieninger, T. Unmüssig, G.A. Urban, Electrochemical characteristics of nanostructured platinum electrodes-A cyclic voltammetry study, PCCP 16 (18) (2014) 8392–8399, https://doi.org/10.1039/c4cp00342j.
[61] J. Perez, E.R. Gonzalez, E.A. Ticianelli, Oxygen electrocatalysis on thin porous coating rotating platinum electrodes, Electrochim. Acta 44 (8–9) (1998) 1329–1339, https://doi.org/10.1016/S0013-4686(98)00255-2.
[62] J. Qi, L. Jiang, M. Jing, Q. Tang, G. Sun, Preparation of Pt/C via a polyol process - Investigation on carbon support adding sequence, Int. J. Hydrogen Energy 36 (17) (2011) 10490–10501, https://doi.org/10.1016/j.ijhydene.2011.06.022.
[63] L. Wang, P. Wurster, P. Gazdzicki, M. Roussel, D.G. Sanchez, L. Guétaz, et al., Investigation of activity and stability of carbon supported oxynitrides with ultra-low Pt concentration as ORR catalyst for PEM fuel cells, J. Electroanal. Chem. 819 (15) (2018) 312–321, https://doi.org/10.1016/j.jelechem.2017.10.067.
[64] C. Wei, S. Sun, D. Mandler, X. Wang, S.Z. Qiao, Z.J. Xu, Approaches for measuring the surface areas of metal oxide electrocatalysts for determining their intrinsic electrocatalytic activity, Chem. Soc. Rev. 48 (9) (2019) 2518–2534, https://doi.org/10.1039/c8cs00848e.
[65] Y. Yang, L.M. Luo, R.H. Zhang, J.J. Du, P.C. Shen, Z.X. Dai, et al., Free-standing ternary PtPdRu nanocatalysts with enhanced activity and durability for methanol electrooxidation, Electrochim. Acta 222 (20) (2016) 1094–1102, https://doi.org/10.1016/j.electacta.2016.11.080.
[66] H. Xu, E.L. Brosha, F.H. Garzon, F. Uribe, M. Wilson, B. Pivovar, The Effect of Electrode Ink Processing and Composition on Catalyst Utilization, ECS Trans. 11 (1) (2007) 383–391, https://doi.org/10.1149/1.2780952.
[67] F. Godínez-Salomón, C.P. Rhodes, K.S. Alcantara, Q. Zhu, S.E. Canton, H.A. Calderon, et al., Tuning the Oxygen Reduction Activity and Stability of Ni$(OH)_2$@Pt/C Catalysts through Controlling Pt Surface Composition, Strain, and Electronic Structure, Electrochim. Acta 247 (1) (2017) 958–969, https://doi.org/10.1016/j.electacta.2017.06.073.
[68] F.J. Vidal-Iglesias, R.M. Arán-Ais, J. Solla-Gullón, E. Herrero, J.M. Feliu, Electrochemical characterization of shape-controlled Pt nanoparticles in different supporting electrolytes, ACS Catal. 2 (5) (2012) 901–910, https://doi.org/10.1021/cs200681x.
[69] H. Shang, W. Sun, R. Sui, J. Pei, L. Zheng, J. Dong, et al., Engineering Isolated Mn-N_2C_2 Atomic Interface Sites for Efficient Bifunctional Oxygen Reduction and Evolution Reaction, Nano Lett. 20 (7) (2020) 5443–5450, https://doi.org/10.1021/acs.nanolett.0c01925.
[70] H. Shang, Z. Jiang, D. Zhou, J. Pei, Y. Wang, J. Dong, et al., Engineering a metal-organic framework derived Mn-N_4-C: XSyatomic interface for highly efficient oxygen reduction reaction, Chem. Sci. 11 (23) (2020) 5994–5999, https://doi.org/10.1039/d0sc02343d.